Journal of Materials Science: Materials in Electronics (2020) 31:3631–3641
https://doi.org/10.1007/s10854-020-02920-y

# Metal–organic framework-derived $ZnMoO_4$ nanosheet arrays for advanced asymmetric supercapacitors

Xiaowei Xu[1] · Cheng Zhao[1] · Xin Liu[1] · Ying Liu[2] · Pei Dong[3] · Connor Itani[3]

Received: 29 October 2019 / Accepted: 16 January 2020 / Published online: 27 January 2020


## Abstract

A metal–organic framework (MOF)-derived $ZnMoO_4$ nanosheets architecture is synthesized on Ni foam using a facile and rapid template-free microwave-assisted hydrothermal approach and subsequent calcination. Further characterizations show that this binder-free electrode is composed of $ZnMoO_4$ nanosheet arrays and, therefore, exhibits an excellent electrochemical performance. The nanosheet array-assembled 3D-frameworks exhibit a maximum-specific capacitance of 1212 F $g^{-1}$ at a current density of 1 A $g^{-1}$, and a good rate capability with a capacitance of 523 F $g^{-1}$ even at a high current density of 20 A $g^{-1}$. Approximately, 93.5% of the maximum-specific capacity is retained, even after 5000 continuous charge–discharge cycles, which exceeds most of $ZnMoO_4$ and $ZnMoO_4$-based electrodes reported so far. A $ZnMoO_4$@Ni foam//GA hybrid device exhibits a maximum-specific capacity of 89 F $g^{-1}$ at a current density of 1 A $g^{-1}$, along with a substantial specific energy of 31.8 W h $kg^{-1}$ at a specific power of 920 W $kg^{-1}$. These results confirmed that the MOF-derived binder-free $ZnMoO_4$ nanosheet arrays are suitable positive electrode materials for hybrid supercapacitors. Our work demonstrates an improved step toward rational design of high-performance integrated electrodes for supercapacitors with a new vision for theoretical and practical applications.

## 1 Introduction

Supercapacitors (SCs) as the most promising renewable energy-storage devices have gained increasing interest because of their rapid charge–discharge rate, high power density, pollution-free operation and long-cycle lifetime [1]. Compared with ion batteries, the low-specific energy density of SCs still hinders their potential applications [2]. The electrochemical properties of SCs are primarily determined by the performances of electrode materials [3]. As electrode materials for SCs, carbonaceous materials (based on an electric double layer principle of physical adsorption) and many metal oxide/hydroxides (involving a fast faradaic process of redox-active species) have been widely explored. Nevertheless, the low-specific capacitances of carbonaceous materials make it difficult to meet the growing demands for electric vehicles and renewable energy [4, 5]. In regard to some transition metal oxides, they are limited in commercials due to high cost, toxicity, and poor electrical conductivity [6, 7]. Therefore, it is still a great challenge for scientists to explore new and advanced capacitive materials with high energy and power density for promising practical applications.

Recently, novel two-dimensional nanostructure materials with good environmental friendliness and enhanced electrochemical properties have been increasingly studied in a number of fields, such as SCs, lithium-ion batteries (LIBs), and catalysis etc. [8–10]. With regard to these standards, metal molybdate materials ($NiMoO_4$, $CoMoO_4$, $MnMoO_4$ etc.) are extremely suited for use in energy-storage devices because of their low cost, environmental friendliness, resourcefulness, and enhanced electrochemical performance compared to the corresponding oxides [11–17]. As a member of the metal molybdate family,

**Electronic supplementary material** The online version of this article (https://doi.org/10.1007/s10854-020-02920-y) contains supplementary material, which is available to authorized users.

✉ Ying Liu
liuying@wtu.edu.cn

Xiaowei Xu
xiaoweixu@sit.edu.cn

[1] School of Materials Science and Engineering, Shanghai Institute of Technology, Shanghai 201418, People's Republic of China

[2] Technological Institute of Wuhan Textile University, Wuhan 430200, People's Republic of China

[3] Department of Mechanical Engineering, George Mason University, Fairfax, VA 22030, USA

$ZnMoO_4$ is expected to possess higher electrochemical performance for the above reasons. Obviously, compared with pure ZnO, the incorporation of Mo atoms can greatly improve the conductivity of $ZnMoO_4$. It has manifested that $ZnMoO_4$ has good catalytic and electrochemical characteristics [18, 19]. For example, Li et al. reported the electrochemical synthesis of ZnO nanorods with a 83 F $g^{-1}$-specific capacitance, and further raised the specific capacitance to 236 F $g^{-1}$ via fabricating ZnO@$MoO_3$ core/shell nanocables; the improvement was for the reason of high dispersibility of $MoO_3$ on the surface of ZnO nanorods and rapid electron transfer of ZnO nanorods [20]. Du et al. demonstrated that ZnO/reduced graphene oxide hybrids obtained the specific capacitance of 231.3 F $g^{-1}$ [21]. Gao et al. also reported $ZnMoO_4$ nanoflowers electrode with the specific capacitance of 704.8 F $g^{-1}$ [22]. Thus, the $ZnMoO_4$ can be identified as one of the most promising electrode materials for the development of high-performances SCs.

In addition, for exploring high-performance electrode materials, well-defined nanoscale subunits of the material architectures can also be an efficient alternative to increase electrochemical kinetics [23]. Currently, metal–organic framework (MOF), known as a new kind of advanced nanomaterials with metal centers as well as organic blocks, has been extensively applied as self-sacrifice template for construction of transition metal oxides and sulfides towards applications on energy storage and -conversion due to the porous structure, high surface area, and rich accessible sites [24–26]. Unfortunately, MOFs with unique geometric structure and high conductivity are highly needed and the electrochemical performances of the derived electrodes still need further improvement. As a result, it is necessary to develop advanced SCs based on MOFs.

Inspired by the above progress, herein, we demonstrate, for the first time, an effective strategy for preparing MOF-derived ultrathin and porous $ZnMoO_4$ nanosheet arrays decorated on three-dimensional Ni foam skeleton using a rapid, simple and economical microwave-assisted hydrothermal method. The MOF-derived $ZnMoO_4$@Ni foam electrode delivers high-specific capacity of up to 1212 F $g^{-1}$ (1 A $g^{-1}$), which is much higher than the commonly used electrodes. Moreover, the electrode material also manifests superb cyclic stability (93.5% capacity retention after 5000 cycles at 15 A $g^{-1}$). In addition, an asymmetric supercapacitor (ASC) device based on this MOF-derived $ZnMoO_4$@Ni foam electrode as positive electrode and graphene aerogel (GA) as negative electrode was evaluated at an operating potential of 1.6 V. Thanks to the high-specific capacity and wide potential of $ZnMoO_4$@Ni foam electrode, the hybrid device obtains an energy density up to 31.8 W h $kg^{-1}$ at a specific power density of 920 W $kg^{-1}$. Furthermore, the hybrid devices demonstrated superb cycle stability with 89% capacitance retention of the initial value even after 5000 cycles.

## 2 Experimental section

### 2.1 Materials

Zinc nitrate hexahydrate (99%), sodium molybdate dehydrate (98%), 2-methylimidazole (98%), ammonium fluoride (96%), potassium hydroxide (85%), and polyethylene glycol 200 (98%) were purchased from Sinopharm Chemical Reagent Co. Ltd (China). Nickel foam (NF) (surface density of 380 g $m^{-2}$, 1.5 mm thick) was purchased from Changsha Lyrun New Material Co. Ltd (China). Before the experiment, Ni foam (6 cm × 2 cm × 0.1 cm) was treated in 6 M HCl solution, ethanol, and acetone under sonication for 30 min, respectively, to remove the impurities and oxide layer on the surface. All reagents used in the experiment were used as received without further purification. All solutions in this study were prepared with deionized water.

### 2.2 Preparation of MOF-derived $ZnMoO_4$@ Ni foam

MOF-derived $ZnMoO_4$@ Ni foam was synthesized using a simple microwave-assisted hydrothermal method. In a typical procedure, 0.82 g of 2-methylimidazole ($C_4H_6N_2$) and 0.59 g of $Zn(NO_3)_2{\cdot}6H_2O$ were dissolved individually in 10 mL of deionized water with 30 min of magnetic stirring at room temperature. After that, the $C_4H_6N_2$ solution was poured into $Zn(NO_3)_2{\cdot}6H_2O$ solution quickly and a piece of pretreated Ni foam was completely immersed into the above-mentioned mixed solution and kept for 1 h. After that, 0.48 g of $Na_2MoO_4{\cdot}2H_2O$ dissolved into 20 mL cosolvent composed of 10 mL deionized water and 10 mL polyethylene glycol 200 (PEG-200) were added into the above mixture solution. Subsequently, 0.07 g of $NH_4F$ was added to the mixture to form transparent solution. The above solution with pretreated Ni foam was transferred into a microwave synthesizer and subjected to microwave heating at 160 °C with a power of 300 W for 30 min. After cooling, the Ni foam depositing with gray sample was cleaned and dried at 60 °C for 8 h. Finally, the Ni foam with MOF-derived $ZnMoO_4$ nanosheet precursor was annealed at 350 °C for 2 h with a slow heating rate of 2 °C $min^{-1}$ in air conditioner to gain final product. For comparison, MOF-absent $ZnMoO_4$ samples were also prepared with the same procedure just without adding 2-methylimidazole.

### 2.3 Materials characterization

The crystallinity of the MOF-derived samples was characterized by X-ray diffraction (XRD, Bruker D/max-γB

diffractometer, Cu Kα source). X-ray photoelectron spectroscopy (XPS) was accomplished on XR 5 VG (UK) spectrometer using Al Kα radiation to investigate the elemental states of the samples. The morphology of the MOF-derived samples were observed via Field-emission scanning electron microscopy (FESEM, Tescan MAIA3), transmission electron microscopy (TEM, JEOL, JEM-2010) and atomic force microscopy (AFM). The $N_2$ adsorption–desorption and pore size distribution were investigated using Brunauer–Emmett–Teller (BET) model and Barrett–Joyner–Halenda (BJH) model.

### 2.4 Fabrication of asymmetric supercapacitor device

A graphene aerogel (GA) electrode was prepared by direct pressing of a piece of grapheme aerogel on Ni foam under 10 MPa pressure. This graphene aerogel-negative electrode was then pressed and combined with a MOF-derived $ZnMoO_4$@Ni foam hybrid-positive electrode with cellulose paper as the separator to fabricate the asymmetric supercapacitor device.

### 2.5 Electrochemical measurement

The electrochemical properties of the MOF-derived $ZnMoO_4$@Ni foam and GA electrodes were investigated in a standard three-electrode system. Saturated calomel electrode (SCE, saturated KCl) and platinum (Pt) wire were used as reference electrode and counter electrode, respectively. The electrochemical performances of ASC were evaluated under a two-electrode system. The cyclic voltammetry (CV) curves, galvanostatic charge–discharge (GCD) curves, and electrochemical impedance spectroscopy (EIS) were recorded on an Autolab PGST128N electrochemical workstation. The specific capacitance (C, F $g^{-1}$) can be calculated by the following formula [27–29]:

$$C = \int I\mathrm{d}V/2vm\Delta V \tag{1}$$

$$C = I\Delta t/m\Delta V \tag{2}$$

where $C$ (F $g^{-1}$) is the specific capacitance, $I$ (A) is the discharge current, $\Delta V$ (V) is the potential difference, $v$ (mV $s^{-1}$) is the potential scan rate, $\Delta t$ (s) is the discharge time, and $m$ (g) is the mass of the electroactive materials.

## 3 Results and discussion

The synthetic process of MOF-derived $ZnMoO_4$ nanosheet arrays on Ni foam involves two steps: the microwave-assisted hydrothermal synthesis of $ZnMoO_4$ precursor through a simple non-redox reaction of Zinc-based MOF and molybdate, then followed by calcination process to obtain MOF-derived binder-free $ZnMoO_4$ nanosheet arrays (Fig. 1). On one hand, 2-methylimidazole ($C_4H_6N_2$) coordinates with $Zn^{2+}$ to form $[Zn–C_4H_6N_2]^{2+}$. Subsequently, the $[Zn–C_4H_6N_2]^{2+}$ further react with $MoO_4^{2-}$ to form $[Zn–C_4H_6N_2]MoO_4$, which finally transform into $ZnMoO_4$ in the later annealing process. On the other hand, PEG-200 with the hydroxyl group (-OH) at both ends of each molecular has hydrogen bond-forming ability and works as a non-ionic surfactant, which is a benefit to the construction of layered morphology. In addition, the high viscosity of PEG-200 leads to the slow diffusion rates of ions, which can greatly suppress the stacking of nanoparticles. Thus, the co-existence of 2-methylimidazole and PEG-200 in the reaction system contributes to the final formation of $ZnMoO_4$ nanosheet arrays.

Figure 2a manifests the typical XRD pattern of the crystallinity of the as-prepared $ZnMoO_4$ nanosheets. It is obvious to see that the sharp diffraction peak at 30.54° comes from the (111) plane reflection of $ZnMoO_4$. The observed other diffraction peaks all could be indexed to the other plane reflections of monoclinic $ZnMoO_4$ (JCPDS card no. 25–1024) very well from its XRD pattern, Raman spectrum (Fig. S1, Supporting Information) and Fourier-transform infrared spectroscopy (FT-IR) spectroscopy (Fig. S2, Supporting Information) [30]. Moreover, there were no extra peaks detected, indicating high purity of the as-obtained $ZnMoO_4$.

The chemical composition and bonding states of $ZnMoO_4$ were analyzed by XPS. It can be seen that the product has a high purity without other impurity peaks (Fig. 2b). Obviously, the main peaks at 1021.4 eV, 530.6 eV, 397.4 eV, 284.8 eV and 232.9 eV can be assigned to Zn 2p, O 1s, Mo 3p, C 1s and Mo 3d, respectively. Figure 2c shows the spectrum of Zn, with a peak at 1021.32 and 1044.46 eV with a 23 eV splitting value. This splitting value was attributed to the Zn $sp_{3/2}$ and Zn $2p_{1/2}$, thereby indicating the existence of $Zn^{2+}$ [31]. The spectrum of Mo 3d is made up of two visible peaks, as shown in Fig. 2d. The two main peaks are the Mo $3d_{5/2}$ (232.38 eV) and Mo $3d_{3/2}$ (235.56 eV) peaks with a splitting of 3.2 eV, manifesting the presence of the $Mo^{6+}$ state [32]. Further, Fig. S3 displays the high-resolution O 1s spectra, in which two peaks with binding energies at 530.7 and 532.6 eV were observed. The O1 peak at 530.7 eV can be identified as a typical metal–oxygen bond (Zn–O) [33]. The fitting $O_2$ peak at 532.6 eV is corresponded to numerous defect sites as well as adsorbed water at the surface [34, 35].

Scanning electron microscopy (SEM) and energy-dispersive X-ray (EDX) mapping were initially employed to investigate the morphologies and distribution of elements of the as-synthesized $ZnMoO_4$ deposited on Ni foam. The SEM images revealed the growth of nanosheets on the 3D

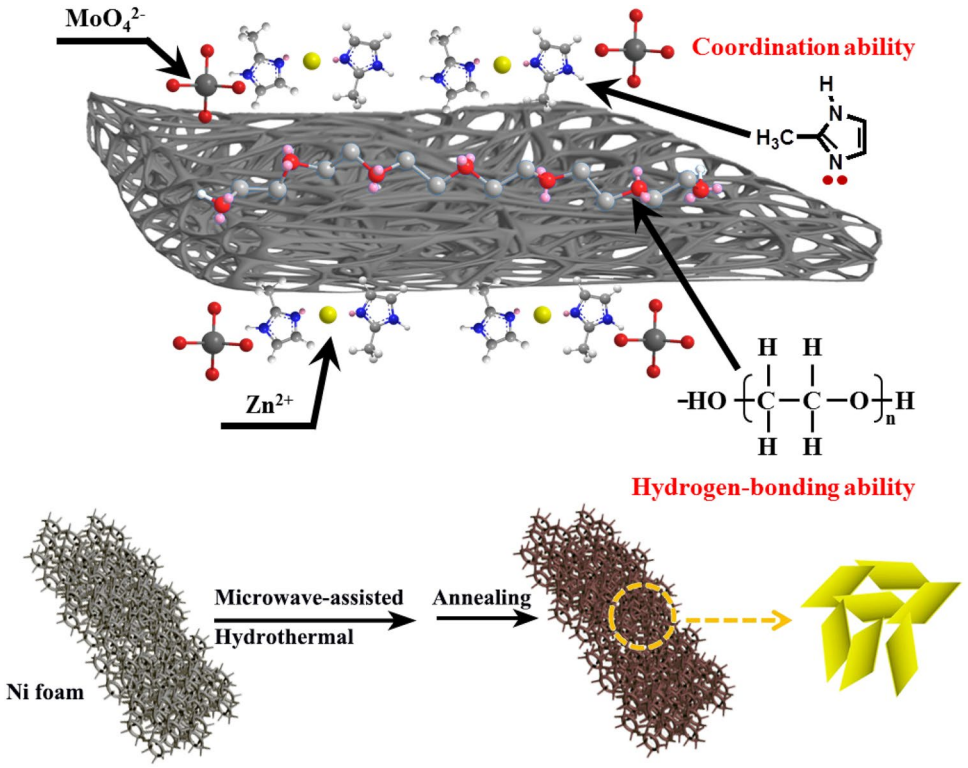


**Fig. 1** Schematic description of growth details of MOF-derived $ZnMoO_4$ nanosheet array-assembled 3D-framworks

porous skeletons of Ni foam. It can clearly be seen that the $ZnMoO_4$ nanosheets are distributed uniformly on the porous Ni foam skeletons (Fig. 3a and b). Figure 3c and d shows the typical SEM images of MOF-derived $ZnMoO_4$ nanosheets supported on the 3D Ni foam substrate under different magnifications. As displayed by SEM images at large magnifications, a unique nanosheet array-like architecture is formed. The diameter and thickness of one nanosheet are around 500 nm and 20 nm, respectively. While the MOF-absent $ZnMoO_4$ samples are composed of plate-like microstructures, these $ZnMoO_4$ microplates appear to be oriented relatively randomly (Fig. S4, Supporting Information). Furthermore, the ultrathin nanosheets of MOF-derived $ZnMoO_4$ possess larger specific surface area than MOF-absent $ZnMoO_4$ microplates (Fig. S5, Supporting Information). The high-specific surface area of MOF-derived $ZnMoO_4$ nanosheets is necessary to expose numerous electrochemically active sites for enhancing SCs performances to some degree. In addition, the adopted microwave heating method ensures strong adhesion between the $ZnMoO_4$ nanosheets and the bare Ni foam. This strong adhesion offers the shortest distance for electron/ion transport, resulting in the highest specific capacitance and best cycle stability. The EDX mapping images (Fig. 3e) manifest that the elements Zn, Mo, and O are uniformly distributed on the surface of materials.

To further explain the morphologies and structural features of the $ZnMoO_4$ nanosheet electrode, the $ZnMoO_4$ nanosheets were separated from Ni foam via ultrasonication and then studied by transmission electron microscopy (TEM). Low magnification TEM images show the nanosheet structure of MOF-derived $ZnMoO_4$ (Fig. 3f) and microplates structure of MOF-absent $ZnMoO_4$ (Fig. S6, Supporting Information), which demonstrates consistency with the SEM results. The height of the $ZnMoO_4$ nanosheet measured by atomic force microscopy (AFM) is around 17 nm, corresponding with ultrathin structure (Fig. S7, Supporting Information). From the HRTEM image (Fig. 3g), a lattice fringe spacing of 0.63 nm could be indexed to the (011) plane reflection of the $ZnMoO_4$. The selected area electron diffraction (SEAD) image (inset of Fig. 3g) of $ZnMoO_4$ displays the diffraction rings, demonstrating the polycrystalline property of the electrode materials, which is consistence with the XRD results. High-angle annular dark-field scanning TEM (HAADF-STEM) was conducted to investigate element distribution of the as-synthesized samples by elemental mapping analysis. The corresponding color maps show a uniform distribution of Zn, Mo, and O throughout the whole nanosheets (Fig. 3h).

The obtained architecture of the prepared $ZnMoO_4$ nanosheets supported on Ni foam was directly applied as binder-free working electrodes. It can be seen that pure Ni foam has essentially little integrated area in comparison with $ZnMoO_4$@Ni foam electrode, demonstrating that the capacitance of pure Ni foam is negligible in this work (Fig. S8, Supporting Information). The CV curves of the as-obtained MOF-derived $ZnMoO_4$ nanosheets and

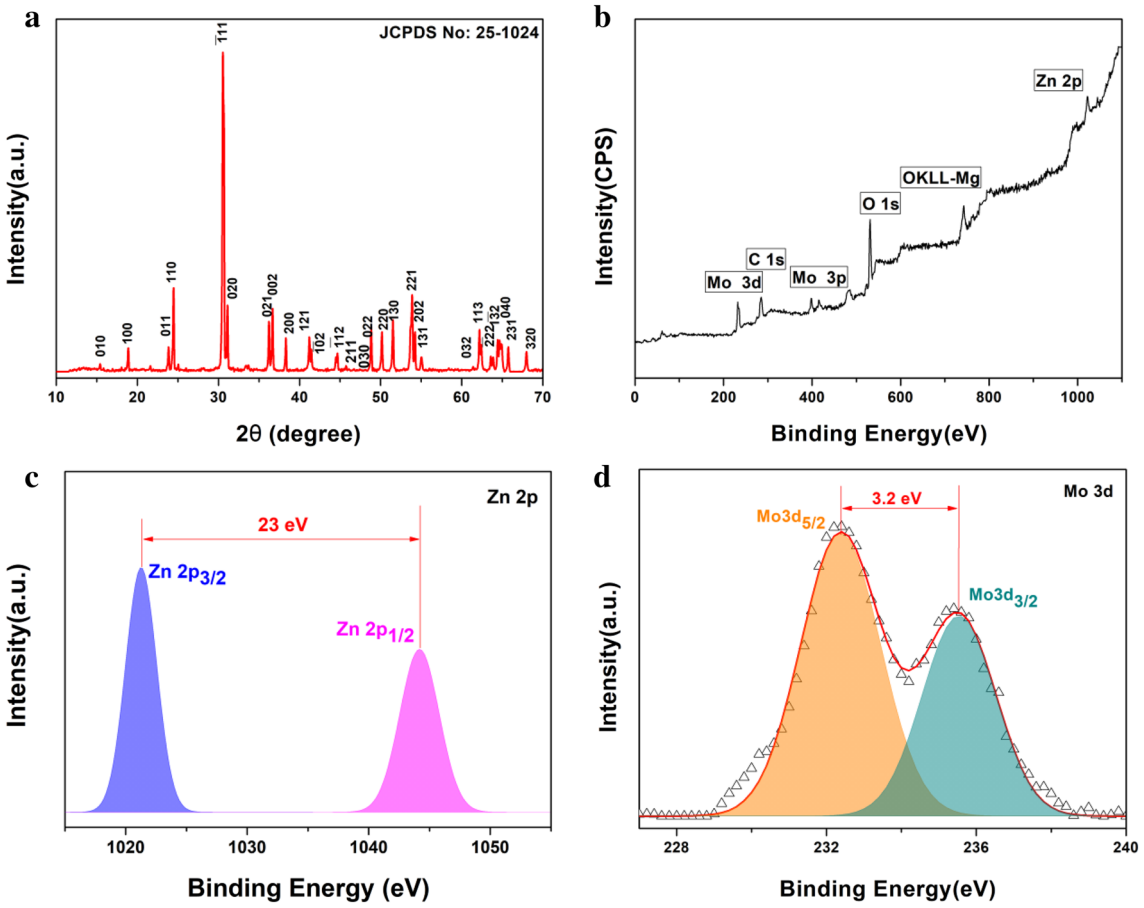


**Fig. 2** **a** XRD patterns, **b** XPS survey spectrum, **c** high-resolution Zn 2p XPS spectrum, and **d** high-resolution Mo 3d XPS spectrum of $ZnMoO_4$

MOF-absent $ZnMoO_4$ microplates as electrode materials in a three-electrode system were collected at different scan rates of 5, 10, 20, 50, 75, and 100 mV $s^{-1}$, as shown in Fig. 4a and Fig. S9a. The obvious redox peaks in each CV curve reveal that the measured capacitances are mainly governed by reversible redox mechanism [36, 37]. The couple of redox peaks in CV curves are similar in nature within the scan rates ranging from 5 to 100 mV $s^{-1}$, which confirm the excellent capacitance behaviors of the MOF-derived $ZnMoO_4$ nanosheets. It can be seen from Fig. 4a that the cathodic peak at 0.30 V is related to the oxidation process, while the anodic peak at 0.45 V is due to its reverse process. In addition, the symmetric characteristic of cathodic and anodic peaks demonstrates the ideal reversibility of the electrode. Obviously, the redox current increased accompanied with the increase of the scan rate from 5 to 100 mV $s^{-1}$ (Fig. 4a), and the cathodic and anodic peaks shift to negative and positive potentials, respectively. As shown in Fig S9b, the specific capacitance of MOF-derived $ZnMoO_4$ nanosheets reached a maximum of about 1437 F $g^{-1}$ at a scan rate of 5 mV $s^{-1}$, which is higher than that of MOF-absent $ZnMoO_4$ microplates (847 F $g^{-1}$). Upon increasing the scan rate from 5 to 100 mV $s^{-1}$, the corresponding specific capacitance gradually decreased. The results show that the low-specific capacitance is due to the slow redox reaction at high scan rate.

The GCD ***measurements were operated at different current densities (1–20 A $g^{-1}$) with voltage range from 0.0 to 0.4 V, and the corresponding curves are shown in Fig. 4b and Fig. S9c. The discharge curves deviate from linearity, indicating the capacitance is mainly based on the faradic redox reactions. Therefore, the existence of plateaus in the charge–discharge curves illustrates the typical pseudocapacitive properties of electrode material, which also supports the CV test results. Furthermore, with increasing the current density, the specific capacitance decreases gradually, which is due to low diffusion of the electrolyte ions at high currents and only some of the electrolyte ions can get access to the active reaction sites, giving rise to a low-specific capacitance [32]. The specific capacitances of MOF-derived $ZnMoO_4$ nanosheets base electrode were 1212, 1106, 954, 645, and 523 F $g^{-1}$ at different current densities of 1, 2, 5, 10, and 20 A $g^{-1}$, respectively, which are much larger than

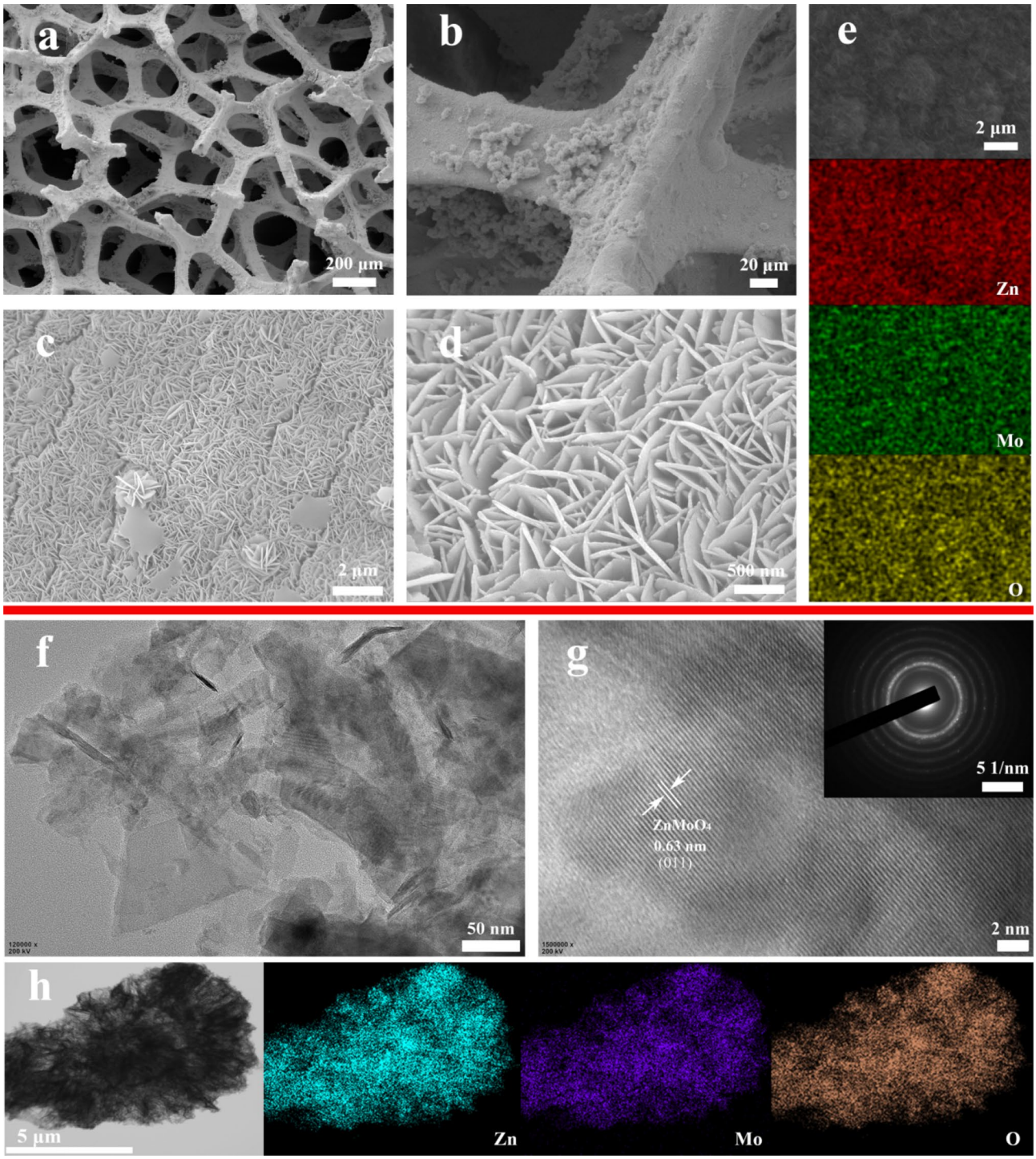


**Fig. 3** **a**, **b** Typical SEM images of Ni foam skeletons loaded with MOF-derived $ZnMoO_4$ nanosheets. **c**, **d** Low and high-magnification SEM images of $ZnMoO_4$ nanosheets. **e** Morphological and corresponding elemental mapping of Zn, Mo, and O. **f**, **g** TEM and HRTEM images of $ZnMoO_4$ nanosheets (inset shows the corresponding SAED pattern). **h** HAADF-STEM image and corresponding elemental mapping of Zn, Mo, and O

that of MOF-absent $ZnMoO_4$ microplates electrodes at the same current densities (Fig. 4c, and Fig. S9d, Supporting Information).

Long-term cyclic stability is also key parameter for the practical applications of SCs. The stability of the $ZnMoO_4$@Ni foam electrode over 5000 times of repeated charge and

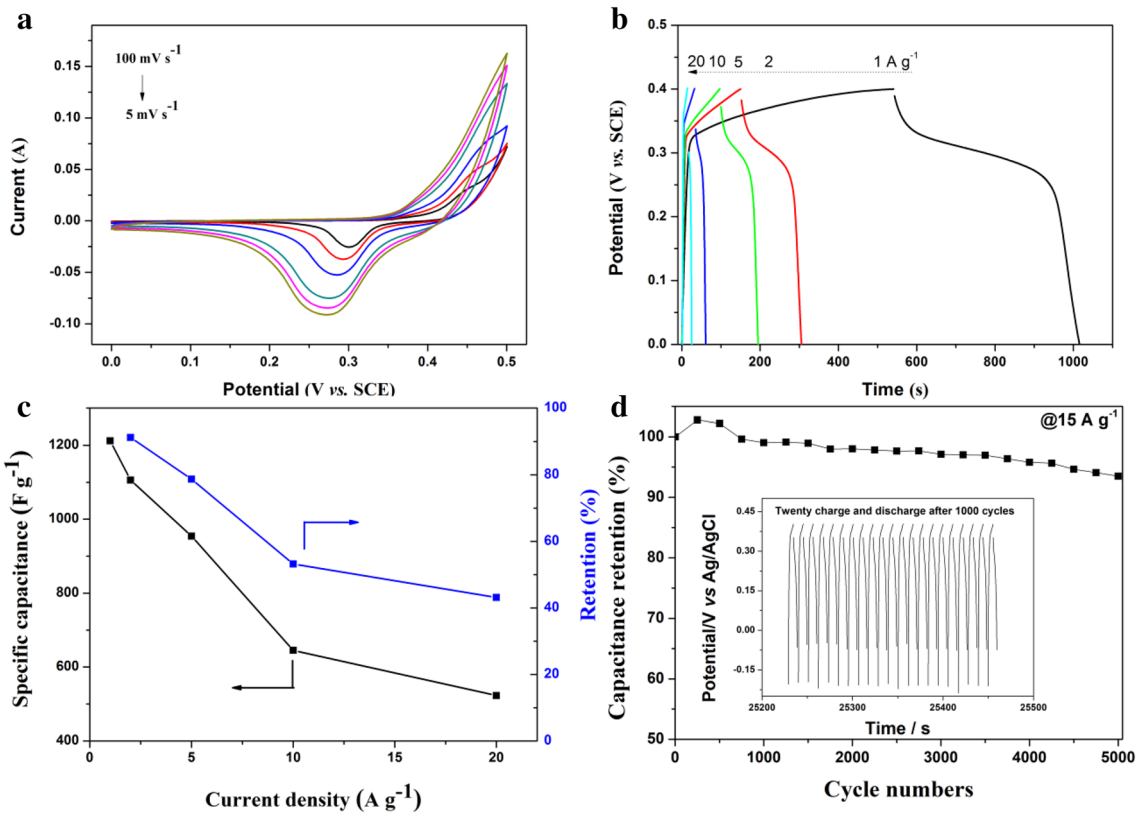


**Fig. 4** Electrochemical performances of MOF-derived $ZnMoO_4$ nanosheet electrode for supercapacitors. **a**, **b** CV and galvanostatic charge/discharge (GCD) curves of $ZnMoO_4$@Ni foam electrode at different scan rates and current densities. **c** Specific capacity and corresponding capacitance retention of $ZnMoO_4$@Ni foam at different current densities. **d** Specific capacitance retention of $ZnMoO_4$@Ni foam as a function of cycle number at 15 A $g^{-1}$ current density

discharge test at 15 A $g^{-1}$ current density is presented in Fig. 4d. It is clearly observed that the capacitance decreases gradually as the cycle proceeding, this could be attributed to aggregation, dissolution, and the collapse of the structure occurred in the electrode material [38]. Furthermore, the EIS measurements after 5000 cycles (Fig. S10, Supporting Information) show an obvious increase in charge transfer resistance. This further leads to the decrease of the specific capacitance during long-term cyclic stability test. Approximately, 93.5% of the specific capacitance retention rate was obtained after 5000 cycles, which exceeds most of $ZnMoO_4$ and $ZnMoO_4$-based electrodes reported so far (Table S1 Supporting Information). In addition, the MOF-derived $ZnMoO_4$ nanosheets unloaded on Ni foam were also tested by conventional binder-needed electrode technology. Due to the application of polymeric binder during electrode fabrication, the transport of ion and electron was largely limited, resulting in poor electrical conductivity between different phases, which is pernicious to the supercapacitor performance (Fig. S10, Supporting Information). It is worth noting that the MOF-derived binder-free $ZnMoO_4$ nanosheet electrode has a low charge transfer resistance compared to the binder-needed counterpart electrode, which further confirms MOF-derived binder-free $ZnMoO_4$ nanosheet electrode has a better electrochemical activity, rapid electron transport kinetics, and diffusion of ions at the interface of electrode/electrolyte. All of the previously mentioned results manifest that the MOF-derived $ZnMoO_4$@Ni foam owed excellent capacitive and long cyclic stability.

To further investigate the possibility of $ZnMoO_4$@Ni foam for real application, an asymmetric supercapacitor (ASC) device was fabricated using a MOF-derived $ZnMoO_4$@Ni foam as anode and the graphene aerogel (GA) as cathode (Fig. 5a). The GA was obtained by a facile hydrothermal method (Fig. S11, Supporting Information). Before fabricating, CV comparisons in each three-electrode systems of both $ZnMoO_4$@Ni foam electrode and GA electrode were measured at the same scan rate of 5 mV $s^{-1}$ (Fig. S12, Supporting Information). Based on the charge balance ($q^+ = q^-$) between the $ZnMoO_4$@Ni foam and GA electrode, the mass ratio of the negative electrode materials to the positive electrode materials is optimized to 2.39. The working voltage window of the $ZnMoO_4$@Ni foam// GA device could be broadened to 1.6 V. The obvious redox

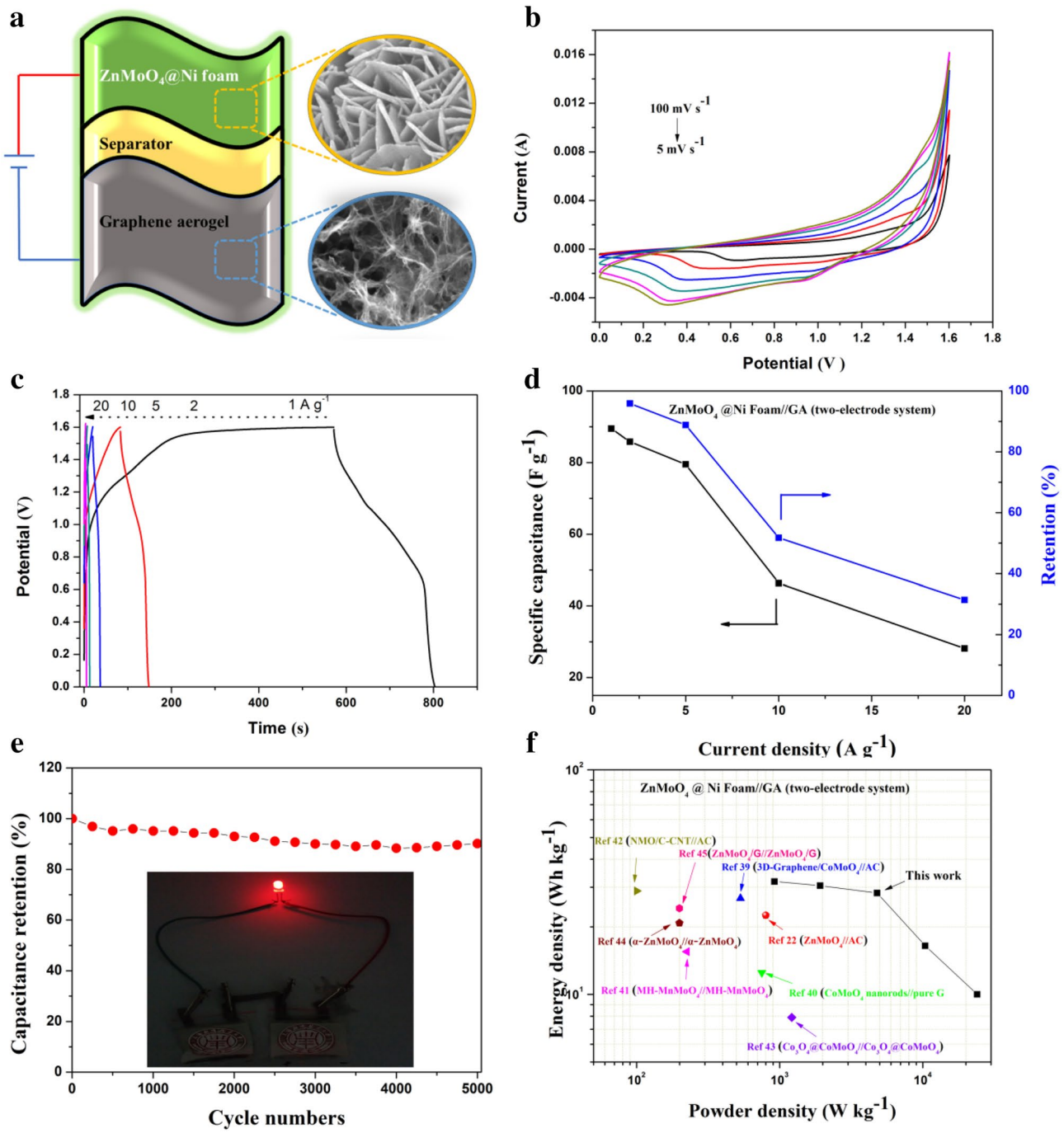


**Fig. 5** Electrochemical evaluation of the $ZnMoO_4$@Ni foam//GA ASC device. **a** Schematic illustration of the ASC device. **b** CV curves of the ASC device at various scan rates from 5 to 100 mV $s^{-1}$ measured between 0 and 1.6 V. **c** Galvanostatic charge/discharge curves at various current densities of the ASC device in the voltage range of 0–1.6 V. **d** Specific capacity and corresponding capacitance retention of the ASC device at different current densities. **e** Cycling performance of the $ZnMoO_4$@Ni foam//GA ASC device (inset shows the real application of two as-prepared ASC devices in series to light up a red LED indicator). **f** Ragone plots of the $ZnMoO_4$@Ni foam-based asymmetric device

peaks still preserved in the CV curves of the ASC device (Fig. 5b), indicating the pseudo-capacitance characteristics owing to the Faradaic reaction of $ZnMoO_4$. Figure 5c shows the GCD plots of the ASC device versus changing current densities. The symmetrical shapes of the GCD curves show the ASC device has good capacitive features and reversibility. The corresponding specific capacitance based on current density is plotted in Fig. 5d. A long-term performance

of the ASC device was studied by a successive GCD test at 15 A $g^{-1}$ for 5000 cycles (Fig. 5e). Benefiting from the integrated structure of $ZnMoO_4$@Ni foam, the ASC device show superb electrochemical stability. After 5000 cycles, the specific capacitance retention rate is still 89%, while Columbic efficiency gradually decreased from 91% before cycling to 78% after cycling. Figure 5f presents the Ragone plots of $ZnMoO_4$@Ni foam//GA device and some typical examples recently reported. The maximum energy density of our $ZnMoO_4$@Ni foam//GA device was 31.8 Wh $kg^{-1}$ at a power density of 920 W$kg^{-1}$, and remains 10 Wh $kg^{-1}$ with a high power density of 24 kW $kg^{-1}$. This is significantly higher than those of previously reported device, such as ZnMoO4//AC (22.45 Wh $kg^{-1}$ at 800 W $kg^{-1}$) [22], 3D-Graphene/CoMoO4//AC (26.8 Wh $kg^{-1}$ at 532.3 W $kg^{-1}$) [39], $CoMoO_4$ nanorods//pure G (12.5 Wh $kg^{-1}$ at 750 W $kg^{-1}$) [40], MH-$MnMoO_4$//MH-$MnMoO_4$ (15.5 Wh $kg^{-1}$ at 224.9 W $kg^{-1}$) [41], NMO/C-CNT//AC (28.9 Wh $kg^{-1}$ at 100 W $kg^{-1}$) [42], $Co_3O_4$@$CoMoO_4$//$Co_3O_4$@$CoMoO_4$ (7.9 Wh $kg^{-1}$ at 1215 W $kg^{-1}$) [43], $\alpha$-$ZnMoO_4$//$\alpha$-$ZnMoO_4$ (20.808 Wh $kg^{-1}$ at 199.44 W $kg^{-1}$) [44], and $ZnMoO_4$/graphene//$ZnMoO_4$/graphene (24.19 Wh $kg^{-1}$ at 199.41 W $kg^{-1}$) [45]. In addition, two $ZnMoO_4$@Ni foam//GA were assembled in series and charged for 20 s to about 3.2 V. The assembled devices can efficiently power a red round light-emitting diode (LED) with 5 mm diameter for more than 2 min (inset of Fig. 5e). The above results highlight the suitability of this $ZnMoO_4$ nanosheet electrode as positive electrode material for SCs.

The superior electrochemical properties could be largely benefited from the unique design of MOF-derived $ZnMoO_4$ nanosheets supported on Ni foam, due to the following three reasons. First, the nanostructure of the sample greatly increases the electrode/electrolyte contact area for reversible faradaic reaction. Second, 3D porous and conductive Ni foam for robust connections to $ZnMoO_4$ provides efficient and short charge transport pathway. Third, a binder-free electrode material with a simple fabricating process has low interface and contact resistances.

## 4 Conclusion

In summary, an integrated electrode with binder-free MOF-derived $ZnMoO_4$ nanosheets on Ni foam has been successfully constructed using a simple and rapid microwave-assisted hydrothermal method. The space between the neighboring nanosheets offers the shortest path length for ion-diffusion which enhances the electrochemical supercapacitor performance. The as-prepared electrode exhibits remarkable electrochemical properties with a high-specific capacitance of 1212 F $g^{-1}$ at a current density of 1 A $g^{-1}$, and outstanding stability (93.5% of initial specific capacitance remained after 5000 cycling). The hybrid device fabricated using $ZnMoO_4$@Ni foam as a positive electrode and GA as a negative electrode exhibited a maximum-specific capacity of 89 F $g^{-1}$ at a current density of 1 A $g^{-1}$. The hybrid $ZnMoO_4$@Ni foam//GA device also exhibited a maximum-specific energy of 31.8 W h $kg^{-1}$ (at a specific power of 920 W $kg^{-1}$) and a maximum-specific power of 24 kW $kg^{-1}$ (at a specific energy of 10 Wh $kg^{-1}$). The high-specific capacity and excellent cycling stability of the MOF-derived $ZnMoO_4$ nanosheets highlight its potential use as a positive electrode material for hybrid supercapacitors. Finally, the present work provides a facile way to design advanced integrated electrodes for novel energy-storage devices in the future.

## 5 Supporting Information

Detailed structural and electrochemical performances of $ZnMoO_4$ nanosheets. This material is available free of charge via the Internet at https://www.sciencedirect.com.

**Acknowledgements** This work was sponsored by Natural Science Foundation of Shanghai (19ZR1455000), Scientific Research Foundation of Shanghai Institute of Technology (YJ2019-14), Hubei knowledge Innovation Project (2019CFC884), Shanghai Engineering Research Center of Building Waterproof Materials (18DZ2253200).

### Compliance with ethical standards

**Conflict of interest** The authors declare no competing financial interest.

## References

1. P. Simon, Y. Gogotsi, Materials for electrochemical capacitors. Nat. Mater. **7**, 845 (2008)
2. H. Chen, S. Chen, Y. Zhu, C. Li, M. Fan, D. Chen, G. Tian, K. Shu, Synergistic effect of Ni and Co ions on molybdates for superior electrochemical performance. Electrochim. Acta **190**, 57–63 (2016)
3. G. Wang, L. Zhang, J. Zhang, A review of electrode materials for electrochemical supercapacitors. Chem. Soc. Rev **41**, 797–828 (2012)
4. T. Stimpfling, F. Leroux, Supercapacitor-type behavior of carbon composite and replica obtained from hybrid layered double hydroxide active container. Chem. Mater. **22**, 974–987 (2010)
5. X. Zhao, B.M. Sánchez, P.J. Dobson, P.S. Grant, The role of nanomaterials in redox-based supercapacitors for next generation energy storage devices. Nanoscale **3**, 839–855 (2011)
6. H. Wang, L. Zhang, X. Tan, C.M.B. Holt, B. Zahiri, B.C. Olsen, D. Mitlin, Supercapacitive properties of hydrothermally synthesized $Co_3O_4$ nanostructures. J. Phys. Chem. C **115**, 17599–17605 (2011)
7. B.-O. Park, C.D. Lokhande, H.-S. Park, K.-D. Jung, O.-S. Joo, Electrodeposited ruthenium oxide ($RuO_2$) films for electrochemical supercapacitors. J. Mater. Sci. **39**, 4313–4317 (2004)

8. E. Kim, D. Son, T.-G. Kim, J. Cho, B. Park, K.-S. Ryu, S.-H. Chang, A mesoporous/crystalline composite material containing tin phosphate for use as the anode in lithium-ion batteries. Angew. Chem. Int. Ed. **43**, 5987–5990 (2004)
9. L. Espinal, S.L. Suib, J.F. Rusling, Electrochemical Catalysis of styrene epoxidation with films of $MnO_2$ nanoparticles and $H_2O_2$. J. Am. Chem. Soc. **126**, 7676–7682 (2004)
10. A.R. Armstrong, P.G. Bruce, Synthesis of layered $LiMnO_2$ as an electrode for rechargeable lithium batteries. Nature **381**, 499 (1996)
11. B. Senthilkumar, K. Vijaya Sankar, R. Kalai Selvan, M. Danielle, M. Manickam, Nano α-$NiMoO_4$ as a new electrode for electrochemical supercapacitors. RSC Adv. **3**, 352–357 (2013)
12. L.-Q. Mai, F. Yang, Y.-L. Zhao, X. Xu, L. Xu, Y.-Z. Luo, Hierarchical $MnMoO_4$/$CoMoO_4$ heterostructured nanowires with enhanced supercapacitor performance. Nat. Commun. **2**, 381 (2011)
13. B. Senthilkumar, D. Meyrick, Y.-S. Lee, R.K. Selvan, Synthesis and improved electrochemical performances of nano β-$NiMoO_4$-$CoMoO_4{\cdot}xH_2O$ composites for asymmetric supercapacitors. RSC Adv. **3**, 16542–16548 (2013)
14. G.Q. Zhang, H.B. Wu, H.E. Hoster, M.B. Chan-Park, X.W. Lou, Single-crystalline $NiCo_2O_4$ nanoneedle arrays grown on conductive substrates as binder-free electrodes for high-performance supercapacitors. Energy Environ. Sci. **5**, 9453–9456 (2012)
15. B. Liu, B. Liu, Q. Wang, X. Wang, Q. Xiang, D. Chen, G. Shen, Correction to new energy storage option: toward $ZnCo_2O_4$ nanorods/nickel foam architectures for high-performance supercapacitors. ACS Appl. Mater. Interfaces **6**, 2199–2199 (2014)
16. D. Guo, P. Zhang, H. Zhang, X. Yu, J. Zhu, Q. Li, T. Wang, $NiMoO_4$ nanowires supported on Ni foam as novel advanced electrodes for supercapacitors. J. Mater. Chem. A **1**, 9024–9027 (2013)
17. X. Yu, B. Lu, Z. Xu, Super long-life supercapacitors based on the construction of nanohoneycomb-like strongly coupled $CoMoO_4$-3D graphene hybrid electrodes. Adv. Mater. **26**, 1044–1051 (2014)
18. H. Fu, J. Lin, L. Zhang, Y. Zhu, Photocatalytic activities of a novel $ZnWO_4$ catalyst prepared by a hydrothermal process. Appl. Catal. A **306**, 58–67 (2006)
19. N.N. Leyzerovich, K.G. Bramnik, T. Buhrmester, H. Ehrenberg, H. Fuess, Electrochemical intercalation of lithium in ternary metal molybdates $MMoO_4$ (M: Cu, Zn, Ni and Fe). J. Power Sources **127**, 76–84 (2004)
20. G.-R. Li, Z.-L. Wang, F.-L. Zheng, Y.-N. Ou, Y.-X. Tong, ZnO@$MoO_3$ core/shell nanocables: facile electrochemical synthesis and enhanced supercapacitor performances. J. Mater. Chem. **21**, 4217–4221 (2011)
21. G. Du, Y. Li, L. Zhang, X. Wang, P. Liu, Y. Feng, X. Sun, Facile self-assembly of honeycomb ZnO particles decorated reduced graphene oxide. Mater. Lett. **128**, 242–244 (2014)
22. Y.-P. Gao, K.-J. Huang, C.-X. Zhang, S.-S. Song, X. Wu, High-performance symmetric supercapacitor based on flower-like zinc molybdate. J. Alloys Compd. **731**, 1151–1158 (2018)
23. Y. Zhao, X. He, R. Chen, Q. Liu, J. Liu, J. Yu, J. Li, H. Zhang, H. Dong, M. Zhang, J. Wang, A flexible all-solid-state asymmetric supercapacitors based on hierarchical carbon cloth@$CoMoO_4$@NiCo layered double hydroxide core-shell heterostructures. Chem. Eng. J. **352**, 29–38 (2018)
24. W.-J. Li, M. Tu, R. Cao, R.A. Fischer, Metal-organic framework thin films: electrochemical fabrication techniques and corresponding applications & perspectives. J. Mater. Chem. A **4**, 12356–12369 (2016)
25. D. Sheberla, J.C. Bachman, J.S. Elias, C.-J. Sun, Y. Shao-Horn, M. Dincă, Conductive MOF electrodes for stable supercapacitors with high areal capacitance. Nat. Mater. **16**, 220 (2016)
26. L. Wang, X. Feng, L. Ren, Q. Piao, J. Zhong, Y. Wang, H. Li, Y. Chen, B. Wang, Flexible solid-state supercapacitor based on a metal-organic framework interwoven by electrochemically-deposited PANI. J. Am. Chem. Soc. **137**, 4920–4923 (2015)
27. P. Shang, J. Zhang, W. Tang, Q. Xu, S. Guo, 2D thin nanoflakes assembled on mesoporous carbon nanorods for enhancing electrocatalysis and for improving asymmetric supercapacitors. Adv. Func. Mater. **26**, 7766–7774 (2016)
28. Z. Li, M. Shao, L. Zhou, R. Zhang, C. Zhang, J. Han, M. Wei, D.G. Evans, X. Duan, A flexible all-solid-state micro-supercapacitor based on hierarchical CuO@layered double hydroxide core-shell nanoarrays. Nano Energy **20**, 294–304 (2016)
29. P. Yuan, C. Cai, J. Tang, Y. Qin, M. Jin, Y. Fu, Z. Li, X. Ma, Anion acceptors dioxaborinane contained in solid state polymer electrolyte: preparation, characterization, and DFT calculations. Adv. Func. Mater. **26**, 5930–5939 (2016)
30. L.S. Cavalcante, E. Moraes, M.A.P. Almeida, C.J. Dalmaschio, N.C. Batista, J.A. Varela, E. Longo, M. Siu Li, J. Andrés, A. Beltrán, A combined theoretical and experimental study of electronic structure and optical properties of β-$ZnMoO_4$ microcrystals. Polyhedron **54**, 13–25 (2013)
31. K. Xiao, L. Xia, G. Liu, S. Wang, L.-X. Ding, H. Wang, Honeycomb-like $NiMoO_4$ ultrathin nanosheet arrays for high-performance electrochemical energy storage. J. Mater. Chem. A **3**, 6128–6135 (2015)
32. D. Ghosh, S. Giri, C.K. Das, Synthesis, characterization and electrochemical performance of graphene decorated with 1D $NiMoO4{\cdot}nH_2O$ nanorods. Nanoscale **5**, 10428–10437 (2013)
33. C. Yuan, J. Li, L. Hou, X. Zhang, L. Shen, X.W. Lou, Ultrathin mesoporous $NiCo_2O_4$ nanosheets supported on Ni foam as advanced electrodes for supercapacitors. Adv. Func. Mater. **22**, 4592–4597 (2012)
34. Y. Lei, J. Li, Y. Wang, L. Gu, Y. Chang, H. Yuan, D. Xiao, Rapid microwave-assisted green synthesis of 3D hierarchical flower-shaped $NiCo_2O_4$ microsphere for high-performance supercapacitor. ACS Appl. Mater. Interfaces **6**, 1773–1780 (2014)
35. R. Zou, K. Xu, T. Wang, G. He, Q. Liu, X. Liu, Z. Zhang, J. Hu, Chain-like $NiCo_2O_4$ nanowires with different exposed reactive planes for high-performance supercapacitors. J. Mater. Chem. A **1**, 8560–8566 (2013)
36. G. Zhang, X.W. Lou, General solution growth of mesoporous $NiCo_2O_4$ nanosheets on various conductive substrates as high-performance electrodes for supercapacitors. Adv. Mater. **25**, 976–979 (2013)
37. B. Qu, Y. Chen, M. Zhang, L. Hu, D. Lei, B. Lu, Q. Li, Y. Wang, L. Chen, T. Wang, β-Cobalt sulfide nanoparticles decorated graphene composite electrodes for high capacity and power supercapacitors. Nanoscale **4**, 7810–7816 (2012)
38. S. Park, S. Kim, Effect of carbon blacks filler addition on electrochemical behaviors of $Co_3O_4$/graphene nanosheets as a supercapacitor electrodes. Electrochim. Acta **89**, 516–522 (2013)
39. Y. Jiang, X. Zheng, X. Yan, Y. Li, X. Zhao, Y. Zhang, 3D architecture of a graphene/$CoMoO_4$ composite for asymmetric supercapacitors usable at various temperatures. J. Colloid Interface Sci. **493**, 42–50 (2017)
40. D.T. Dam, T. Huang, J.-M. Lee, Ultra-small and low crystalline $CoMoO_4$ nanorods for electrochemical capacitors. Sustain. Energy Fuels **1**, 324–335 (2017)
41. S. Jayasubramaniyan, S. Balasundari, P.A. Rayjada, N. Satyanarayana, P. Muralidharan, Microwave hydrothermal synthesis of α-$MnMoO_4$ nanorods for high electrochemical performance supercapacitors. RSC Adv. **8**, 22559–22568 (2018)
42. B. Tong, W. Wei, X. Chen, J. Wang, W. Ye, S. Cui, W. Chen, L. Mi, Designed synthesis of porous $NiMoO_4$/C composite nanorods for asymmetric supercapacitors. CrystEngComm **21**, 5492–5499 (2019)

43. J. Wang, X. Zhang, Q. Wei, H. Lv, Y. Tian, Z. Tong, X. Liu, J. Hao, H. Qu, J. Zhao, Y. Li, L. Mai, 3D self-supported nanopine forest-like $Co_3O_4$@$CoMoO_4$ core–shell architectures for high-energy solid state supercapacitors. Nano Energy **19**, 222–233 (2016)
44. B.J. Reddy, P. Vickraman, A.S. Justin, A facile synthesis of novel α-$ZnMoO_4$ microspheres as electrode material for supercapacitor applications. Bull. Mater. Sci. **42**, 52 (2019)
45. B.J. Reddy, P. Vickraman, A.S. Justin, Investigation of novel zinc molybdate-graphene nanocomposite for supercapacitor applications. Appl. Phys. A **124**, 409 (2018)